

those made using other types of detectors.

An image of the phase-matched harmonic output was obtained by placing an imaging microchannel plate detector (XSI) before the spectrometer at a distance of 0.68 m from the output of the capillary. The observed harmonic beam images for harmonics 23 to 31 are shown (Fig. 4). Figure 4A shows the harmonic output beam, which is not phase-matched, at low pressures. Because in the absence of phase-matching the harmonic generation is not associated with any one particular mode of the wave guide, the beam quality is poor. In contrast, Fig. 4B shows the output harmonic beam at a pressure of 35 torr, when phase-matching is optimized. Because the fundamental wave guide mode is now phase-matched to create the x-ray output, the x-rays generated have excellent spatial properties. The grid pattern which is apparent on the image is due to the  $\sim 27$  lines/cm mesh on which the x-ray filter is mounted. The x-ray beam full-width-at-half-maximum diameter is  $\approx 1$  mm. Given our source distance of 0.68 m and the source size of radius  $\approx 20$   $\mu\text{m}$ , the measured diffraction angle of  $\sim 1$  mrad is consistent with a near-diffraction-limited x-ray output beam.

In future experiments, more optimal laser-fiber coupling, larger diameter fibers (which reduce absorption loss), lower absorption gases, and use of shorter pulses should allow significant increases in the efficiency of the phase-matched harmonic conversion process. By using recent advances in laser technology, it should be straightforward to generate milliwatts of power per harmonic peak. It should also be possible to apply this technique to shorter wavelengths, thus enabling a wide variety of new experimental investigations in linear and nonlinear x-ray science.

## REFERENCES AND NOTES

- P. A. Franken, A. E. Hill, C. W. Peters, G. Weinreich, *Phys. Rev. Lett.* **7**, 118 (1961).
- C. Tang, W. Bosenberg, T. Ukachi, R. Lane, L. Cheng, *Proc. IEEE* **80**, 365 (1992).
- P. Di-Trapani *et al.*, *J. Opt. Soc. Am. B* **14**, 1245 (1997).
- L. Myers *et al.*, *ibid.* **12**, 2102 (1995).
- U. Heitmann, M. Kotteritzsch, S. Heitz, A. Hese, *Appl. Phys. B* **55**, 419 (1992).
- A. L'Huillier and P. Balcou, *Phys. Rev. Lett.* **70**, 774 (1993).
- J. Zhou, J. Peatross, M. M. Murnane, H. C. Kapteyn, I. P. Christov, *ibid.* **76**, 752 (1996).
- Z. Chang, A. Rundquist, H. Wang, M. M. Murnane, H. C. Kapteyn, *ibid.* **79**, 2967 (1997).
- Ch. Spielmann *et al.*, *Science* **278**, 661 (1997).
- P. B. Corkum, N. H. Burnett, M. Y. Ivanov, *Opt. Lett.* **19**, 1870 (1994).
- I. P. Christov, M. M. Murnane, H. C. Kapteyn, *Phys. Rev. Lett.* **78**, 1251 (1997).
- P. Antoine *et al.*, *Phys. Rev. A* **56**, 4960 (1997).
- C. Kan, C. Capjack, R. Rankin, T. Brabec, N. Burnett, *ibid.* **54**, R1026-0 (1996).
- A. L'Huillier, X. Li, L. Lompre, *J. Opt. Soc. Am. B* **7**, 527 (1990).
- S. C. Rae, K. Burnett, J. Cooper, *Phys. Rev. A* **50**, 3438 (1994).
- A. H. Kung, J. F. Young, S. E. Harris, *Appl. Phys. Lett.* **22**, 301 (1973).
- R. Mahon, T. J. McIlrath, V. P. Myerscough, D. W. Koopman, *IEEE J. Quantum Electron.* **QE-15**, 444 (1979).
- A. L'Huillier, K. J. Schafer, K. C. Kulander, *Phys. Rev. Lett.* **66**, 2200 (1991).
- H. Milchberg, C. Durfee III, T. McIlrath, *ibid.* **75**, 2494 (1995).
- C. G. Durfee, S. Backus, M. M. Murnane, H. C. Kapteyn, *Opt. Lett.* **22**, 1565 (1997).
- E. A. J. Marcatelli and R. A. Schmeltzer, *Bell Syst. Tech. J.* **43**, 1783 (1964).
- S. Backus, C. G. Durfee, G. A. Mourou, H. C. Kapteyn, M. M. Murnane, *Opt. Lett.* **22**, 1256 (1997).
- M. T. Asaki *et al.*, *ibid.* **18**, 977 (1993).
- We gratefully acknowledge support from NSF. H.C.K. acknowledges support from an Alfred P. Sloan Foundation Fellowship.

23 February 1998; accepted 13 April 1998

## Electrical Conductivity of Olivine, Wadsleyite, and Ringwoodite Under Upper-Mantle Conditions

Yousheng Xu,\* Brent T. Poe, Thomas J. Shankland,† David C. Rubie

Geophysical models show that electrical conductivity in Earth's mantle rises about two orders of magnitude through the transition zone in the depth range 410 to 660 kilometers. Impedance measurements obtained on  $\text{Mg}_{1.8}\text{Fe}_{0.2}\text{SiO}_4$  olivine, wadsleyite, and ringwoodite at up to 20 gigapascals and 1400°C show that the electrical conductivities of wadsleyite and ringwoodite are similar and are almost two orders of magnitude higher than that of olivine. A conductivity-depth profile to 660 kilometers, based on these laboratory data, shows a conductivity increase of almost two orders of magnitude across the 410-kilometer discontinuity; such a profile favors a two-layer model for the upper mantle. Activation enthalpies of 1.2 to 1.7 electron volts permit appreciable lateral variations of conductivity with lateral temperature variations.

Estimates of the mineralogy, composition, and temperature of Earth's mantle come mainly from comparisons of seismic velocity data with measurements of the elasticity and density of potential mantle minerals (1). Refinements of such estimates can be derived by comparing electrical conductivity models with laboratory measurements of the conductivity of proposed mantle minerals (2–5). Electrical conductivity as a function of depth is calculated by inverting geomagnetic and magnetotelluric data, but such data can be fit to a range of models in which conductivity either varies smoothly with depth or changes abruptly at certain depths. In the latter case, models have been proposed in which conductivity increases rapidly, for example, at depths of 410 km (2),  $\sim 500$  km (3, 4), and  $\sim 660$  km (3, 4).

One reason for uncertainties in the electrical conductivity of the mantle is the lack of laboratory measurements on transition-zone minerals. In the depth range 410 to 660 km, the most abundant upper-mantle mineral,  $\text{Mg}_{1.8}\text{Fe}_{0.2}\text{SiO}_4$  olivine, transforms to

the high-pressure polymorphs wadsleyite ( $\sim 410$  km depth) and ringwoodite ( $\sim 520$  km) and then disproportionates to  $(\text{Mg,Fe})\text{-SiO}_3$  perovskite +  $(\text{Mg,Fe})\text{O}$  ( $\sim 660$  km). Olivine conductivity has been measured at 1 bar and at pressures to 5 GPa (6). Omura (7) measured the conductivities of wadsleyite and ringwoodite with expected mantle compositions,  $\text{Fe}/(\text{Mg} + \text{Fe}) \approx 0.1$ . These results, which suggest that conductivity increases by a factor of  $\sim 2$  at the olivine-wadsleyite transition and by  $\sim 5$  for a wadsleyite-ringwoodite transition, have been debated on the basis of experimental complications (8).

We have measured conductivities of  $\text{Mg}_{1.8}\text{Fe}_{0.2}\text{SiO}_4$  olivine, wadsleyite, and ringwoodite up to 20 GPa and 1400°C within their respective stability fields (Fig. 1) (9, 10). The starting material was San Carlos olivine  $\text{Mg}_{1.8}\text{Fe}_{0.2}\text{SiO}_4$  to which 5 weight %  $\text{Mg}_{0.915}\text{Fe}_{0.085}\text{SiO}_3$  orthopyroxene was added to buffer silica activity. The small volume fraction of pyroxene has little influence on bulk conductivity. To minimize changes in the sample geometry at high pressures and iron loss to the electrodes during extended periods at high temperatures, we synthesized the polycrystalline samples in separate hot-pressing experiments and, in the case of high-pressure phases, phase-transformation experiments (11).

Bayerisches Geoinstitut, Universität Bayreuth, D-95440 Bayreuth, Germany.

\*To whom correspondence should be addressed. E-mail: yousheng.xu@uni-bayreuth.de

†On leave from Earth and Environmental Sciences Division, Los Alamos National Laboratory, Los Alamos, NM 87545, USA.

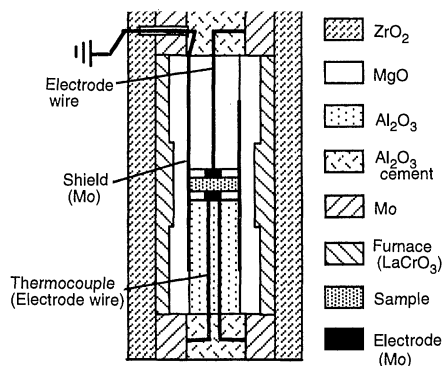


**Fig. 1.** Schematic cross-section of high-pressure cell assembly for complex impedance measurements in the multi-anvil press. Experiments up to 10 GPa (olivine) were carried out in 18-mm octahedral assemblies, to 15 GPa (wadsleyite) in 14-mm octahedra, and to 20 GPa (ringwoodite) in 10-mm octahedra. Recovered assemblies show that geometrical distortions are small and introduce errors of less than 12%. Temperature uncertainty is  $\pm 15^\circ\text{C}$ .

Impedance spectroscopy was used to determine sample conductance and to distinguish different conduction paths in the sample environment (Fig. 2) (12, 13). Mo electrodes were used so that oxygen fugacity could be close to the Mo-MoO<sub>2</sub> buffer, which is similar to that for iron-wüstite (14). Conductivities were fit to the equation

$$\sigma = \sigma_0 \exp(-\Delta H/kT) \quad (1)$$

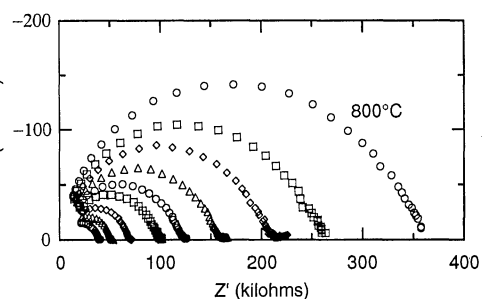
where  $\sigma_0$  is a preexponential factor,  $T$  is temperature,  $k$  is the Boltzmann constant, and the activation enthalpy  $\Delta H = \Delta U + P\Delta V$  (where  $\Delta U$  is activation energy,  $\Delta V$  is activation volume, and  $P$  is pressure).

The conductivities of polycrystalline olivine sample H813 at three different pressures are similar to those of a single-crystal olivine, H811, along the [100] direction, and to a reference curve consistent with polycrystalline and single-crystal olivine at 1 atm (Fig. 3A) (6). The electrical conductivity of H813 decreases slightly with increasing pressure, and it has an activation volume of 0.68 cm<sup>3</sup>/mol, which is not sig-

nificantly different from zero.  $\Delta H$  is about 1.7 eV at high pressure, and calculated zero-pressure activation energy is 1.62 eV (Table 1). The weak pressure effect on olivine conductivity is consistent with previous studies (5, 15). The wadsleyite and ringwoodite conductivities are similar to each other, and both are about two orders of magnitude higher than that of olivine (Fig. 3B and Table 1).

The conductivity jump we determined (about a factor of 100) at the olivine-wadsleyite transition is greater than the factor of 2 jump determined by Omura (7), and the net conductivity jump (about a factor of 100) for the overall olivine-ringwoodite transition is also greater than the factor of 10 jump reported by Omura (7). We believe that the different results arise from experimental complications in the earlier measurements (16).

Our thermoelectric measurements (12) indicate positive charge carriers in the range 1000° to 1400°C for olivine up to 10 GPa and for wadsleyite to 15 GPa. If conduction in wadsleyite and the structurally similar ringwoodite is controlled by the positive small polaron Fe<sup>3+</sup> favored for olivine (17), then the greater conductivity of the high-pressure phases could come from two causes. The first cause would be higher Fe<sup>3+</sup> abundance, as expected in these phases from the data of O'Neill *et al.* (18), but still below our Mössbauer detection limit for



nificantly different from zero.  $\Delta H$  is about 1.7 eV at high pressure, and calculated zero-pressure activation energy is 1.62 eV (Table 1). The weak pressure effect on olivine conductivity is consistent with previous studies (5, 15). The wadsleyite and ringwoodite conductivities are similar to each other, and both are about two orders of magnitude higher than that of olivine (Fig. 3B and Table 1).

Fe<sup>3+</sup>/(Fe<sup>2+</sup> + Fe<sup>3+</sup>) of  $\sim 0.02$ . The second cause would be shorter hopping distances between neighboring cations in wadsleyite than in olivine (19), an effect inferred for the conductivity increase at the olivine-tospinel transition in Mg<sub>2</sub>GeO<sub>4</sub> (20). In addition, the nearly identical conductivities of wadsleyite and ringwoodite are consistent with their similar crystal structures (21).

Olivine and its high-pressure polymorphs are considered to be volumetrically the most abundant minerals in the upper mantle (22) and are therefore likely to gov-

**Table 1.** Activation energies and preexponential terms from fitting Eq. 1 to the experimental data. Fitting Eq. 1 to olivine data (H813) to include the pressure effect yields the results:  $\log \sigma_0 = 2.69 \pm 0.12$ ;  $\sigma_0 = 490 \text{ S/m}$ ;  $\Delta U = 1.62 \pm 0.04 \text{ eV}$ ;  $\Delta V = 0.68 \pm 0.14 \text{ cm}^3/\text{mol}$ .

Mineral	Sample	$P$ (GPa)	$T$ (°C)	$\log \sigma_0$	$\sigma_0$ (S/m)	$\Delta H$ (eV)
Olivine	H813	4	1000–1300	$2.98 \pm 0.17$	955	$1.73 \pm 0.05$
		7	1000–1400	$2.63 \pm 0.19$	427	$1.66 \pm 0.05$
		10	1000–1400	$2.71 \pm 0.18$	513	$1.69 \pm 0.05$
Single-crystal olivine, [100]	H811	10	1000–1400	$3.02 \pm 0.22$	1047	$1.71 \pm 0.06$
Wadsleyite	H613	15	800–1200	$2.04 \pm 0.15$	110	$0.95 \pm 0.04$
Ringwoodite	H564	20	1050–1200	$3.29 \pm 0.20$	1950	$1.29 \pm 0.06$
			800–1200	$2.92 \pm 0.04$	832	$1.16 \pm 0.01$

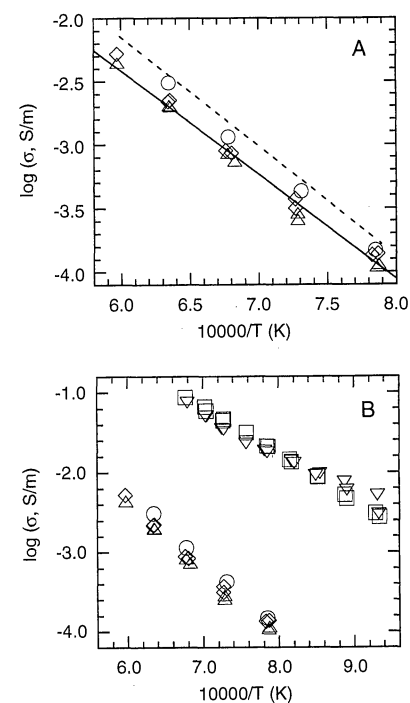
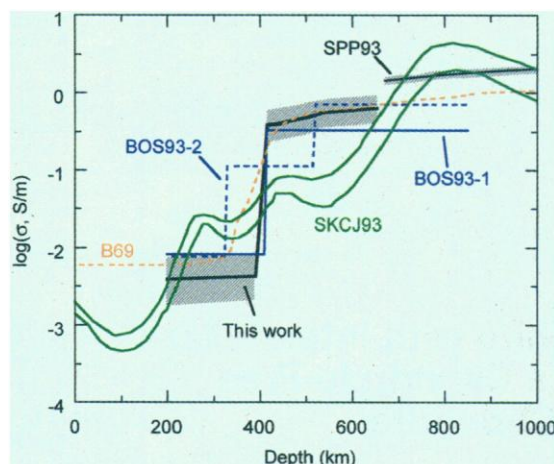


**Fig. 3.** (A) Electrical conductivity of olivine as a function of reciprocal temperature. Circles, diamonds, and triangles denote H813 at 4, 7, and 10 GPa, respectively. The dashed line represents H811 at 4 GPa, and the solid line shows the SO<sub>2</sub> model. (B) Electrical conductivity of olivine (H813), wadsleyite, and ringwoodite as a function of reciprocal temperature. Circles, diamonds, and triangles are the same as in (A). Inverted triangles denote wadsleyite at 15 GPa; squares denote ringwoodite at 20 GPa.

**Fig. 4.** Conductivity model for the upper mantle calculated from our laboratory data (black thick line) with the addition of a lower mantle curve for perovskite + magnesiowüstite having bulk iron fraction  $Fe/(Fe + Mg) = 0.11$  [SPP93 (black thick line) (25)]. Shaded areas illustrate the effect on the model of a  $\pm 100^\circ\text{C}$  temperature variation. Geophysical models are shown as B69 (red) (2), BOS93-1 (blue) (2), BOS93-2 (blue) (2), and SKCJ93 (green) (3). The estimated uncertainty in the laboratory-based model is  $\pm 0.3$  log units.



ern its bulk electrical conductivity. We can construct a conductivity-depth profile from Eq. 1 using the data from Table 1. Temperatures as a function of depth are from (23) for 390 to 660 km and are extrapolated to 200 km along a temperature gradient of  $0.3^\circ\text{C}$  per kilometer (24). To simplify this laboratory-based conductivity model, we do not consider any activation volume for the transition-zone minerals, nor effects of oxygen fugacity, possible OH in the minerals, the presence of other mineral phases, and texture. These factors can have opposing influences and may contribute a  $\pm 0.3$  order of magnitude uncertainty in the calculated conductivities. Because the finite depths over which phase transitions occur at 410, 520, and 660 km are not likely to be resolved in geophysical profiles, we do not attempt to include the refinement of calculating mixed-phase regions associated with the transitions.

Figure 4 compares the resulting model with geophysical models. The two-layer (BOS93-1) and three-layer (BOS93-2) models were obtained from magnetotelluric/geomagnetic data from Western Europe by a Monte Carlo inversion (2). Schultz *et al.* (3) found three discrete zones of conductivity increase beneath the central Canadian Shield by using long-period magnetotelluric data (SKCJ93 model). Geophysical models show that conductivity is on the order of 1 S/m at the top of the lower mantle. To complete the laboratory model, we show a portion of the outermost lower mantle for perovskite + magnesiowüstite transformed from  $Mg_{1.78}Fe_{0.22}SiO_4$  [SPP93 (25)]. Comparing our laboratory-based model with the lower-mantle models B69 (2), BOS93-1 (2), and SKCJ93 (3) indicates that the change in conductivity at 660 km is expected to be relatively small. Although uncertainties in the laboratory-based model are on the order of  $\pm 0.3$  log units, the laboratory model is closer to the

two-layer model BOS93-1 than to the three-layer models BOS93-2 and SKCJ93 (2, 3). For the SKCJ93 three-layer model, Schultz *et al.* (3) mentioned that a conductivity jump of about two orders of magnitude between 400 and 550 km could also fit the data. Our experiments indicate that the olivine-wadsleyite phase transition at 410 km could be the primary cause of this jump.

Our results indicate a conductivity increase of two orders of magnitude at the olivine-wadsleyite transformation (410 km discontinuity) and a minor increase where wadsleyite transforms to ringwoodite at  $\sim 520$  km depth. The change in conductivity at the 660-km discontinuity is also expected to be small. These experimental data favor step-like conductivity increases at mineral phase boundaries. The shaded areas in Fig. 4 show the conductivity variation in the laboratory-based model when temperature is allowed to vary by  $\pm 100^\circ$ . Because  $\Delta H$  is large in upper-mantle minerals, strong lateral variations of conductivity are possible as a consequence of lateral temperature variations between upwelling and downwelling convection limbs.

#### REFERENCES AND NOTES

1. T. S. Duffy and D. L. Anderson, *J. Geophys. Res.* **94**, 1895 (1989); T. S. Duffy, C. S. Zha, R. T. Downs, H. K. Mao, R. J. Hemley, *Nature* **378**, 170 (1995).
2. R. J. Banks, *Geophys. J. R. Astron. Soc.* **17**, 457 (1969) [B69]; K. Bahr, N. Olsen, T. J. Shankland, *Geophys. Res. Lett.* **20**, 2937 (1993) [BOS93-1 and BOS93-2].
3. A. Schultz, *Phys. Earth Planet. Inter.* **64**, 68 (1990); ———, R. D. Kurtz, A. D. Chave, A. G. Jones, *Geophys. Res. Lett.* **20**, 2941 (1993) [SKCJ93].
4. H. F. Peterson and S. Constable, *Geophys. Res. Lett.* **23**, 1461 (1996).
5. A. Duba, H. C. Heard, R. N. Schock, *J. Geophys. Res.* **79**, 1667 (1974); S. Constable, *J. Geomagn. Geoelectr.* **45**, 707 (1993).
6. S. Constable and A. Duba, *J. Geophys. Res.* **95**, 6967 (1990); T. J. Shankland and A. G. Duba, *Geophys. J. Int.* **103**, 25 (1990); J. J. Roberts and J. A. Tyburczy, *J. Geophys. Res.* **96**, 16205 (1991); S. Constable, T. J. Shankland, A. Duba, *ibid.* **97**, 3397 (1992); A. Duba and S. Constable, *ibid.* **98**, 11885 (1993) [SO2]; L. M. Hirsch, T. J. Shankland, A. G. Duba, *Geophys. J. Int.* **114**, 36 (1993).
7. K. Omura, *Phys. Earth Planet. Inter.* **65**, 292 (1991).
8. A. Duba and J. von der Gönna, *ibid.* **82**, 75 (1994); K. Omura, *ibid.*, p. 79.
9. Pressure was calibrated at high temperature with olivine-wadsleyite-ringwoodite transitions in  $Mg_2SiO_4$  and the quartz-coesite-stishovite transitions (10). Temperatures were measured with a Pt-Pt<sub>90</sub>Rh<sub>10</sub> thermocouple without correcting the measured electromotive force for effects of pressure.
10. D. C. Rubie, C. R. Ross II, M. R. Carroll, S. C. Elphick, *Am. Mineral.* **78**, 574 (1993); D. Canil, *Phys. Earth Planet. Inter.* **86**, 25 (1994).
11. Polycrystalline olivine, wadsleyite, and ringwoodite samples were prepared by hot-pressing olivine powder (Mo capsule) in the multi-anvil apparatus for 2.5 hours at  $1200^\circ\text{C}$  and 4, 15, and 20 GPa, respectively. After hot-pressing, the samples were prepared as disks about 1.55 mm in diameter and 0.40 mm thick, and the polished faces showed no detectable iron loss. The samples were characterized by x-ray diffraction, electron microprobe analysis, and optical microscopic examination and showed no evidence of minor phases. One single-crystal sample of olivine (*a*-axis orientation) was also used. After the sample was placed inside the octahedral pressure medium, the whole cell assembly was dried overnight at  $225^\circ\text{C}$  in a vacuum furnace. After measurements, microscopic examinations showed no grain size changes, and geometric distortions were small so that they introduced maximum uncertainties of 12%. Mössbauer spectra were acquired for some synthesized specimens.
12. To overcome such high-pressure and high-temperature experimental difficulties as leakage current and electrical disturbance from the furnace, we used a parallel electrode method with a Mo shield connected to ground (Fig. 1). Advantages of the shield include filtering electrical disturbances from the furnace, reducing temperature gradients, reducing leakage current through the pressure medium, and blocking reactions between sample and pressure medium. For impedance spectroscopy, we used a Solartron 1260 impedance-gain phase analyzer with 1 V applied voltage over the frequency range 10 mHz to 1 MHz. This method gives results identical to in-circuit impedance measurements because major leakage current paths in parallel with the sample are excluded by virtual earth guarding through the grounded shield. Thermoelectric measurements were made on separate samples for which two thermocouples were used to measure an imposed thermal gradient.
13. Y. Xu, B. T. Poe, D. C. Rubie, in *The Review of High Pressure Science and Technology, Proceedings of JOINT AIRAPT-16 & HPCJ-38*, vol. 7, M. Nakahara, Ed. (Japan Society of High-Pressure Science and Technology, Kyoto, Japan, 1998), pp. 1526–1528.
14. C. H. P. Lupis, *Chemical Thermodynamics of Materials* (North-Holland, New York, 1983), p. 134.
15. R. N. Schock, A. G. Duba, H. C. Heard, H. D. Stromberg, in *High Pressure Research, Applications in Geophysics*, M. H. Manghni and S. Akimoto, Eds. (Academic Press, San Diego, CA, 1977), pp. 39–51.
16. Complications in (7) include the following: (i) Leakage paths divert currents through high-conductivity reaction products between the sample and pressure medium (8). (ii) The oxidation state of the sample during the measurement could not be well defined (8). (iii) Iron loss to the electrodes during hot-pressing before the conductivity measurements inhibited current flow through the sample. We also performed one experiment in which wadsleyite was synthesized from olivine and its electrical conductivity measured in the same experiment, a procedure similar to Omura's. This experiment showed a conductivity increase of only a factor of  $\sim 3$  at the olivine-wadsleyite transition, which resembles Omura's result (7). Because the sample recovered after this procedure showed severe iron loss to the electrodes from a zone  $\sim 10 \mu\text{m}$  thick on each side, we rejected the results of this experiment. Analyses of the samples in

Fig. 3 showed no iron loss.

17. R. N. Schock, A. G. Duba, T. J. Shankland, *J. Geophys. Res.* **94**, 5829 (1989); S. Constable and J. J. Roberts, *Phys. Chem. Miner.* **24**, 319 (1997).
18. H. St. C. O'Neill et al., *Am. Mineral.* **78**, 456 (1993).
19. B. Kamb, *ibid.* **53**, 1439 (1968).
20. G. Nover, G. Will, R. Waitz, *Phys. Chem. Miner.* **19**, 133 (1992).
21. H. Horiuchi, M. Akaoki, H. Sawamoto, in *High-Pressure Research in Geophysics*, S. Akimoto and M. H. Manghnani, Eds. (Center for Academic Publications, Tokyo, 1982), pp. 391–403.
22. A. E. Ringwood, *Composition and Petrology of the Earth's Mantle* (McGraw-Hill, New York, 1975), p. 618; T. Irifune and A. E. Ringwood, *Earth Planet. Sci. Lett.* **86**, 365 (1987).
23. E. Ito and T. Katsura, *Geophys. Res. Lett.* **16**, 425 (1989).
24. D. L. Turcotte and G. Schubert, *Geodynamics: Applications of Continuum Physics to Geological Problems* (Wiley, New York, 1982).
25. T. J. Shankland, J. Peyronneau, J.-P. Poirier, *Nature* **366**, 453 (1993) [SPP93].
26. We thank A. G. Duba and H. Xie for discussions and

suggestions; H. Fischer, K. Klasinski, H. Kufner, and R. Weigel for technical assistance; and H. Schulze for making the thin sections. D. L. Kohlstedt (University of Minnesota) donated sample materials. Electron microprobe analyses were performed with the assistance of D. Kraube, and C. McCammon and S. Lauterbach did the Mössbauer analyses of the samples. T.J.S. thanks the Alexander von Humboldt Foundation and the Office of Basic Energy Sciences of the U.S. Department of Energy for support.

28 January 1998; accepted 23 March 1998

## In Situ Discovery of Graphite with Interstellar Isotopic Signatures in a Chondrule-Free Clast in an L3 Chondrite

S. Mostefaoui, P. Hoppe, A. El Goresy\*

Optical and scanning electron microscopy of a chondrule-free clast in the unequilibrated L3 chondrite Khohar revealed a spherical object consisting of an aggregate of small (~2-micrometer diameter), Ni-poor (0.5 to 2.89 weight percent) metal particles and fine-grained graphite (<1-micrometer diameter). The graphite has large D and <sup>15</sup>N excesses (δD ~ 1500 per mil and δ<sup>15</sup>N ~ 1300 per mil) with two isotopically distinct signatures: N rich with a high D/H ratio and N poor with a high <sup>15</sup>N/<sup>14</sup>N ratio. These excesses are the largest D and <sup>15</sup>N excesses observed in situ in a well-characterized phase in a meteorite. The isotopic characteristics are suggestive of an interstellar origin, probably by ion-molecule reactions at low temperature in the interstellar molecular cloud from which the solar system formed. The structure and nonchondritic composition of the metal particles suggest they did not form under equilibrium conditions in the solar nebula.

Different graphite morphologies (1) have been observed in many unequilibrated chondrites (2, 3). In the unequilibrated ordinary chondrite Khohar (UOC L3 type) and the Acfer-182 carbonaceous chondrite of Renazzo type (CR), large <sup>15</sup>N and D excesses were measured in mixtures of fine-grained graphite and graphite books (book refers to a structure of parallel sheets) (2). The large size of the books permitted analysis of individual grains by secondary ion mass spectrometry (SIMS). The H and N isotopic compositions did not indicate any <sup>15</sup>N or D excesses; however, we could not analyze the different fine-grained graphite grains separately because the graphite grain types are mixed with the graphite books. To determine if the fine-grained graphite grains are the source of the <sup>15</sup>N and D anomalies, we searched for assemblages that contained only the fine-grained graphite to analyze for C, N, and H isotopic compositions.

In a fine-grained chondrule-free clast in the Khohar chondrite (Fig. 1A) we found a

S. Mostefaoui and A. El Goresy, Max-Planck-Institut für Kernphysik, Postfach 103980, 69029 Heidelberg, Germany.

P. Hoppe, Physikalisches Institut, Universität Bern, Sidlerstrasse 5, CH-3012 Bern, Switzerland, and Max Planck-Institut für Chemie, Postfach 3060, D-55020 Mainz, Germany.

\*To whom correspondence should be addressed. E-mail: goresy@pluto.mpi-hd.mpg.de

spherical object (~100 μm in diameter) consisting of an unaltered fine-grained, Ni-poor metal aggregate and graphite (Fig. 1B). This spherule does not have layers surrounding it, and the graphite was found to be all fine grained. We analyzed the whole clast for its bulk chemical composition with the electron microprobe (EMP) broad-beam technique. The graphite-bearing metal spherule was then surveyed with a scanning electron microscope (SEM), and the metal phases were analyzed for Fe, Ni, Co,

Cr, Si, P, and S by wavelength-dispersive EMP techniques. The isotopic compositions of H, C, and N of the graphite were measured by SIMS.

The clast is about 2 mm in diameter and essentially chondrule free (Fig. 1A). Because the clast is located at the edge of the meteorite section, its original size was probably larger. The clast consists mostly of small (<10 μm) silicate grains and metal particles, with some large metal grains (~100 μm) and two glass grains (~300 μm) (Fig. 1A). The bulk chemical composition of the clast (Table 1), obtained by 20 broad-beam EMP analyses, is different from the bulk compositions of both the Khohar chondrite and the L ordinary chondrite group (4). The abundances of the major oxides SiO<sub>2</sub>, MgO, and FeO are similar to those of the bulk composition of the Orgueil (CI) carbonaceous chondrite (Table 1).

The metal-graphite assemblage in the clast (Fig. 1, B and C) consists of small (≤2 μm) metal particles of kamacite and taenite and fine-grained (<1 μm) birefringent graphite (5). Detailed examination of the metals with high-resolution BSE imaging with the SEM revealed no sign of alteration of the metal. The graphite is abundant and fills interstices between the metal particles (Fig. 1D). We estimated the total amount of C in the assemblage to be about 50 volume %. This much graphite with its

**Table 1.** The bulk chemical composition of the chondrule-free clast in the Khohar (L3) chondrite. The Khohar chondrite, L group ordinary chondrites (OCs), and Orgueil (CI) carbonaceous chondrite bulk chemical compositions are shown for comparison.

Compound	Khohar clast		Orgueil (bulk)	Khohar (bulk)	L group OCs (bulk)
	Range	Average			
SiO <sub>2</sub>	37.24–44.41	40.82	37.90	46.71	46.7
TiO <sub>2</sub>	0.11–1.37	0.21	0.12	0.13	0.14
Al <sub>2</sub> O <sub>3</sub>	2.39–3.49	2.87	2.84	2.70	2.64
Cr <sub>2</sub> O <sub>3</sub>	0.48–0.85	0.69	0.53	0.61	0.62
FeO	22.54–26.66	25.07	28.11	16.83	17
MnO	0.36–0.47	0.42	0.35	0.41	0.4
MgO	24.61–27.22	26.11	26.51	29.31	29.07
CaO	0.56–3.59	1.38	2.27	2.11	2.17
Na <sub>2</sub> O	0.53–1.03	0.77	1.27	1.05	1.12
K <sub>2</sub> O	0.20–0.46	0.36	0.10	0.12	0.13
Total	97.54–101.52	98.71	100.00*	100.00*	100.00*

\*Recalculated from (4), after subtraction of H<sub>2</sub>O, P<sub>2</sub>O<sub>5</sub>, C, FeS, and Fe-Ni-Co metal.